OPEN ACCESS

University of Dundee

University of Dundee

A Weighted Average Phase Velocity Inversion Model for Depth-Resolved Elasticity Evaluation in Human Skin In-Vivo

Zhou, Kanheng; Feng, Kairui; Li, Chunhui; Huang, Zhihong

Link to publication in Discovery Research Portal

A Weighted Average Phase Velocity Inversion Model for Depth-Resolved Elasticity Evaluation in Human Skin *In-Vivo*

Kanheng Zhou[#], Kairui Feng[#], Chunhui Li[*] and Zhihong Huang

Abstract— *Objective:* **In current surface acoustic wave (SAW) elastography field, wavelength-depth inversion model is a straightforward and widely used inversion model for depth-resolved elasticity profile reconstruction. However, the elasticity directly evaluated from the wavelength-depth relationship is biased. Thus, a new inversion model, termed weighted average phase velocity (WAPV) inversion model, is proposed to provide depth-resolved Young's modulus estimate with better accuracy.** *Methods:* **The forward model for SAW phase velocity dispersion curve generation was derived from the numerical simulations of SAWs in layered materials, and inversion was implemented by matching the measured phase velocity dispersion curve to the one generated from the forward model using the least squares fitting. Three two-layer agar phantoms with different top-layer thicknesses and one three-layer agar phantom were tested to validate the proposed inversion model. Then the model was demonstrated on human skin at various sites (palm, forearm and back of hand)** *in-vivo*. *Results:* **In multi-layered agar phantoms, depth-resolved elasticity estimates provided by the model have a maximal total inversion error of 15.2% per sample after inversion error compensation. In** *in-vivo* **human skin, the quantified bulk Young's moduli (palm: 212 ± 78 kPa; forearm: 32 ± 11 kPa and back of hand: 29 ± 8 kPa) are comparable to the reference values in the literature.** *Conclusion:* **The WAPV inversion model can provide accurate depth-resolved Young's modulus estimates in layered biological soft tissues.** *Significance:* **The proposed model can predict depth-resolved elasticity in layered biological soft tissues with a reasonable accuracy which traditional wavelength-depth inversion model cannot provide.**

Index Terms— **Elastography, inversion model, optical coherence tomography, surface acoustic waves.**

I. INTRODUCTION

S KIN, as the largest organ of our human body, is significantly important owing to its functions, including immune surveillance, thermoregulation and sensory detection [1]. The mechanical property of skin, specifically Young's modulus, is closely related to its pathophysiological conditions. For example, the skin elasticity of a systemic sclerosis patient is 1.7 ~ 5.9 times higher than that of a normal person [2]. Besides,

K. Zhou, K. Feng, and Z, Huang are with School of Science and Engineering, University of Dundee
C. Li is with School of Science and Engineering, University of Dundee, Dundee, DD1 4HN, UK (email: c.li@dundee.ac.uk)
[#] These authors contribute equally to this work.

with ageing in normal skin, skin becomes stiffer [3, 4]. Thus, quantitative evaluation of the mechanical property of skin is of great importance for skin disease diagnosis and skin health management.

Surface acoustic wave optical coherence elastography (SAW-OCE) utilises the propagation behaviour of SAW captured by optical coherence tomography (OCT) for quantification of the mechanical property of soft tissues. The typical procedure for a SAW-OCE test consists of 1) launching a broadband SAW along air-sample interface; 2) tracking the propagating SAW with M-B mode OCT scanning; 3) frequency-dependent SAW phase velocity dispersion curve reconstruction using the spatial-temporal axial displacement field extracted from the sample surface; 4) depth-resolved elasticity profile evaluation with wavelength-depth inversion model [5-7]. Previous studies in SAW-OCE have proven the feasibility of depth-resolved elasticity profile reconstruction in *in-vivo* and *ex-vivo* skin samples through the wavelength-depth inversion model [5-7]. Although the dispersion curve roughly indicates vertical elasticity change in the material, the elasticity directly converted from the wavelength-depth relationship is biased. Therefore, a new inversion model is required to a provide accurate depth-resolved elasticity estimates.

In seismology, the dispersive behaviour of SAW layered materials has been extensively studied. Different techniques have been used to forward model this problem, involving ray theory, propagator matrix method, finite difference method and finite element method [8]. However, most forward models based on complex wave equations are computationally expensive and require a long time to be solved in the inversion stage. To mitigate this problem, Leong *et al*. [9] proposed a computationally efficient model. They hypothesized the SAW phase velocity at a specific wavelength in the dispersion curve as a weighted average of the shear wave velocities of the layers within one wavelength depth. The proposed weighted average forward model was successfully demonstrated in soil with different structures. In soft materials, this hypothesis is also feasible, as Mohan *et al*. [10] successfully predicted the depth-resolved elasticity profiles in two-layer tissue phantoms and *ex-vivo* tissues.

In this paper, we will present a novel and reliable inversion model based on the above hypothesis, termed weighted average phase velocity (WAPV) inversion model, for depth-resolved elasticity evaluation in multi-layered biological soft tissues,

such as human skin. The proposed WAPV inversion model was firstly validated in multi-layered tissue mimicking phantoms and then demonstrated in human skin *in vivo*.

II. Weighted Average Phase Velocity Inversion Model

A. Forward model

A forward model is a model that takes certain parameters and produces data that can be compared with the actual observations. In this study, a forward model that predicts the frequency-dependent SAW phase velocity, $C_R(f)$, was proposed based on 1) the numerical solutions of the wave equations describing the propagation of SAW in multi-layered materials and 2) the hypothesis in [9].

1) Forward equations

In a multi-layered material, the SAW phase velocity at a specific wavelength, $C_R(\lambda)$, can be expressed as:

$$C_R(\lambda) = \left(\frac{0.87+1.12\upsilon}{1+\upsilon} \right) \sum_{i=1}^{N} W_i(\lambda) \cdot C_{S(i)} \tag{1}$$

$$\sum_{i=1}^{N} W_i(\lambda)=1 \quad (0<W_i(\lambda)<1) \tag{2}$$

where υ is the Poisson's ratio, N represents the number of total layers, $W_i(\lambda)$ represents the weight of the ith layer at the specific wavelength λ, and $C_{S(i)}$ denotes the shear wave velocity of the ith layer. In this study, the wavelength-dependent weighting function $W_i(\lambda)$ was determined from the average of a series of numerical solutions of SAW propagation in layered, nearly incompressible materials, which can be expressed as:

$$W_i(\lambda)=\frac{\int_{Z_{i-1}}^{Z_i} k(\frac{z}{\lambda})dz}{\int_0^{1.425\lambda} k(\frac{z}{\lambda})dz} \tag{3}$$

where Z_{i-1} represents the depth from the surface to the top of the ith layer, and Z_i denotes the depth from the surface to the bottom of the ith layer. The integral kernel $k(z/\lambda)$ in (3) is given by:

$$\begin{cases} k(\frac{z}{\lambda})=ABe^{B\frac{z}{\lambda}}+CDe^{D\frac{z}{\lambda}}+EFe^{F\frac{z}{\lambda}} & (\frac{z}{\lambda}\leq1.425) \\ k(\frac{z}{\lambda})=0 & (\frac{z}{\lambda}>1.425) \end{cases} \tag{4}$$

where parameters A to F equal to -6, -3.329, 5, -3.766, 1 and 0.02005, separately.

To achieve a robust weighting function, behaviours of SAW in layered materials with different top-layer thicknesses (0.1 mm, 0.3 mm, 0.6 mm, 1.0 mm and 2.0 mm) and various top-bottom shear wave velocity ratios ($\frac{8}{7}$ to $\frac{8}{1}$ with a decrement of 1 in the denominator) were explored by numerical simulations. The applied top-layer thicknesses cover the typical layer thicknesses of skin tissues at different sites. Besides, the employed top-bottom shear wave velocity ratios range from 1.14 to 8, corresponding to top-bottom Young's modulus ratios of 1.3 to 64, which also include most situations either in normal skin tissues at different sites or in diseased skin tissues at various disease stages. Numerical simulations and the derivation of the weighting function are described in detail in Section A and B in the online supplementary document, respectively.

Based on (1), (3) and (4), the wavelength-dependent SAW phase velocities in a multi-layered material can be reconstructed. By converting wavelength to frequency, the frequency-dependent SAW phase velocity dispersion curve $C_R(f)$ can be finally generated from the proposed forward model.

2) Model Interpretation

In the proposed forward model, the SAW phase velocity at a specific wavelength was modeled as a weighted average of the shear wave velocities in the layers within 1.425 wavelength depth, where the weight of each layer was calculated as the ratio of the area enclosed by the integral kernel in each layer to the total area under the integral kernel, e.g., $A_i(\lambda_i)/[A_1(\lambda_i) + A_2(\lambda_i) + \cdots + A_N(\lambda_i)]$, as shown in Fig. 1(a). It is reasonable to estimate the weighting factor of each layer in this way as previous research in seismology suggests the wavelength-dependent SAW phase velocity is influenced by the shear wave velocity of each layer it penetrates into, and the amount of influence from each layer could be in 'approximate' proportion to the relative amount of vibrations that occur within each layer [11].
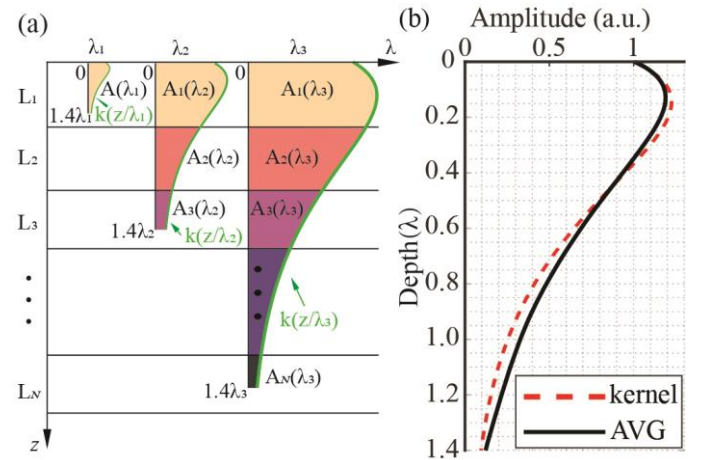

Fig. 1. (a) Illustration of the wavelength-dependent weighting function in a multi-layered material (Frequency low to high) (b) Comparison between the integral kernel function (red dashed line) and the normalised, averaged SAW axial displacement profile of different layer thickness (black solid line). The axial displacement was normalised with the displacement at surface (z=0), and the depth was normalised with the measured SAW wavelength.

Furthermore, the integral kernel $k(z/\lambda)$ can be interpreted as the fundamental mode SAW axial displacement profile along depth [9, 10]. There is a good agreement between the integral kernel function and the normalised, averaged SAW axial displacement profile from the numerical simulation, as show in Fig. 1(b). The comparison between the integral kernel and the SAW axial displacement profile of each configuration of the numerical simulation is shown in Section C in the online supplementary document.

B. Inversion

Based on the proposed forward model, the shear wave velocity of each layer can then be estimated by matching the SAW phase velocity dispersion curve generated from the model with the one measured in the experiment using the least squares fitting. The root-mean-square error (RMSE) was employed as the objective function in the inversion, which can be expressed as:

$$F_{obj} = \sqrt{\frac{\sum_{i=1}^{n}\left(C_R(f)-\hat{C}_R(f)\right)^2}{n}} \qquad (5)$$

where $C_R(f)$ and $\hat{C}_R(f)$ are the frequency-dependent SAW phase velocity measured in the experiment and generated by the forward model, respectively, and n is number of data points. By searching the minimal RMSE value in the selected range for the variables in the forward function, the best fitting can be obtained, thus giving the optimal shear wave velocity estimates for each layer. The corresponding coefficient of determination (R^2) of the besting fitting can written as:

$$R^2 = 1 - \frac{\sum(C_R(f)-\hat{C}_R(f))^2}{\sum(C_R(f)-\overline{C}_R(f))^2} \qquad (6)$$

where $\overline{C}_R(f)$ denotes the mean value of the measured frequency-dependent SAW phase velocity. For a layered material with N independent homogeneous transverse layers, there are $2N$-1 variables, including N-1 variables for the layer thickness and N variables for the corresponding shear wave velocity. To reduce the fitting complexity, layer thicknesses were pre-defined during the fitting, where the thickness of each layer was directly measured from the OCT structure image. Thus, only the shear wave velocity of each layer was changed during iteration.

After the optimal shear wave velocity of each layer, $C_{S(i)}$, was obtained from the fitting, the Young's modulus of each layer E_i can then be quantified using the following equation:

$$E_i = 3\rho C_{S(i)}^2 \qquad (7)$$

Here, ρ represents the mass density of the material.

III. MATERIALS AND METHODS

A. Sample preparation

1) Multi-layered agar phantom

Agar phantom was employed to validate the proposed inversion models in this study. The general protocol for producing the agar phantom has been described in detail in our previous study [12]. Three two-layer agar phantoms with different top-layer thicknesses and one three-layer agar phantom were produced.

Two-layer agar phantoms were made from 3% (top layer) and 2% (bottom layer) agar solutions. Top layers with different thickness were made first by pouring 3% agar solution into round plastic Moulds $A_{1\sim3}$ with designed thickness of 0.5, 1 and 2 mm, respectively. After cured, they were carefully transferred to Mould B, which have the same diameter as Mould A but with deeper depth. Then, bottom layers were produced by pouring 2% agar solution onto top layers. The finished phantom had a size of 9 cm in diameter and 1.2 cm in height. Three top-layer thicknesses were measured by OCT to be 0.45 mm, 1.00 mm and 2.00 mm, respectively.

The three-layer agar phantom was made from 3% (top layer), 2% (middle layer) and 1% (bottom) agar solutions. The protocol for fabricating three-layer agar phantom was similar to that for two-layer agar phantom. The finished three-layer agar phantom had the same overall size of the two-layer one. The thicknesses of top and middle layers were measured by OCT to be 0.63 mm and 1.10 mm, respectively.

2) In-vivo human skin

To explore the feasibility and performance of the proposed WAPV inversion model in the in-vivo human skin, eleven healthy adults (6 males and 5 females, age: 22 – 36 years old) were enrolled in this study. The study was approved by the School of Science and Engineering Research Ethics Committee (SSEREC) of the University of Dundee, which also conformed to the tenets of the Declaration of Helsinki. Informed consent was obtained from each subject prior to the SAW imaging.

B. Experimental setup

1) SAW generation

A piezoelectric actuator (PC4QR, Thorlabs Inc., Newton, NJ, USA) was employed in this study for SAW generation. During the experiment, the piezoelectric actuator was put tilted at an angle of 45° above the sample to not block the laser beam from the OCT system. A 3D printed actuator head was attached to the work plane of the actuator to transmit the vibration from the piezo material onto the sample surface to generate mechanical waves. A 2-mm-diameter rod at the end of the actuator head works as a line source. The contact length between the actuator head and the sample surface depends on the preload between the actuator head and sample surface, which was typically 0.5 mm when the actuator head was pressed about 30 µm (5 ~ 6 pixels in OCT structure image) into the sample. In multi-layered agar phantom experiment, the actuator was driven by a 4-ms burst chirp signal with frequency ranging from 0.1 to 25 kHz, while in in-vivo human skin experiment, the frequency range was selected to be 0.1 ~ 7 kHz. This frequency range was determined based on the maximal SAW bandwidth observed from human skin in experiments. The actuator head had a maximum peak positive amplitude of 250 nm to avoid phase wrapping in the acquired data.

2) SAW detection

A M-B mode phase-sensitive OCT system (PhS-OCT) [13] with central wavelength of 1310 nm and an A-line rate of 92 kHz was applied for SAW detection in this study. The axial resolution of the system is 6.89 µm in air with an axial sampling distance of 4.7 µm/pixel, while the transverse resolution of the system is 23.5 µm in air with a lateral sampling distance of 21.7 µm/pixel. The maximum penetration depth of this system was ~2 mm in agar phantom and ~1 mm in human skin. The transverse image range was 11 mm, and the recorded time length was 5.5 ms. It took 3.9s for each data acquisition.

For each sample in the multi-layered agar phantom experiment, 32 repeated acquisitions were performed and averaged for sensitivity enhancement. To obtain the reference SAW velocity in each homogeneous layer, additional datasets were acquired on the homogeneous phantoms fabricated from the 1% to 3% agar solutions of the same batch. Each homogeneous phantom was also repeatedly measured 32 times. In the in-vivo human skin experiment, each subject was scanned on three locations, e.g., palm, forearm and back of hand, and each location was repeatedly tested 3 times. All data was acquired through a customized LabVIEW interface (LabView 2010, National Instruments, Austin, TX, USA) and stored in the computer for postprocessing.

C. Data processing

All acquired datasets went through a 2D-FFT analysis using a customized MATLAB script (MATLAB 2017, MathWorks Inc., Natick, MA, USA) for SAW phase velocity dispersion curve reconstruction, which has been described in detail in the previous study [7]. The reconstructed SAW phase velocity dispersion curve along with the layer thickness measured from OCT structure image by pixel counting was then input into the proposed WAPV inversion model for depth-resolved Young's modulus evaluation.

IV. RESULTS

A. Multi-layered agar phantom experiment

The reconstructed phase velocity dispersion curve (black solid line) for each multi-layered agar phantom is shown in Fig. 2.
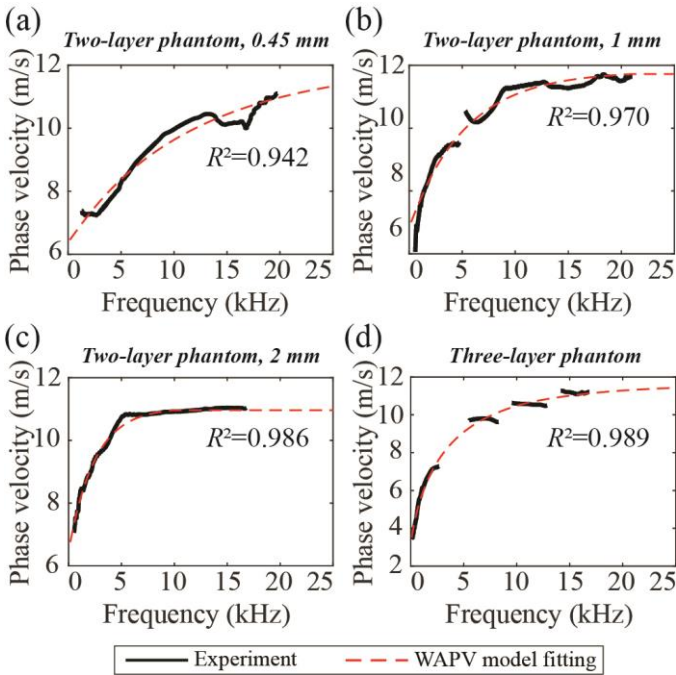

Fig. 2. Reconstructed SAW phase velocity dispersion curve with its best WAPV model fitting in (a) the two-layer agar phantom with the top-layer thickness of 0.45 mm; (b) the two-layer agar phantom with a top-layer thickness of 1.0 mm; (c) the two-layer agar phantom with a top-layer thickness of 2.0 mm; and (d) the three-layer agar phantom.

As illustrated in the figure, the phase velocity approaches and stabilizes at a constant value, e.g., the SAW velocity of the top layer, when the wavelength of the SAW is roughly smaller than the top-layer thickness. As the wavelength has an inverse relationship with the frequency (for a constant wave speed), the frequency at which the SAW phase velocity stabilizes increases as the top layer gets thinner. For instance, the phase-velocity-stabilizing frequency in the two-layer agar phantom with top-layer thickness of 2.0 mm (Fig. 2(c)) is 5.1 kHz (wavelength of 2.1 mm), while this frequency increases to 9.2 kHz (wavelength of 1.2 mm) when the top-layer thickness reduces to 1.0 mm (Fig. 2(b)). In the two-layer phantom with the top-layer thickness of 0.45 mm (Fig. 2(a)), the phase-velocity-stabilizing frequency was approximated to be 26.2 kHz according to $f = C_R/\lambda$, thus, the phase velocity does not stabilize even at the highest frequency available on the dispersion curve.

In the three-layer agar phantom (Fig. 2(d)), the reconstructed phase velocity curve is intermittent as the existing high order SAW modes interfere with the fundamental mode. Thus, the fundamental-mode phase velocities at some frequencies were biased. To mitigate this problem, the biased fundamental mode phase velocity estimates, i.e., phase velocities obtained from high order SAW modes, were manually picked and removed.

The red dashed lines in Fig. 2 present the best fitting results for the measured dispersion curve in each phantom with the R^2 value annotated. All R^2 values are higher than 0.94. Table 1 summarises the evaluated depth-resolved Young's moduli, reference values and the corresponding estimation errors of each multi-layered agar phantom. Please note that the Young's modulus reference value of each layer was calculated based on the shear wave velocity of each layer using (7), where the shear wave velocity of each layer was measured using time-of-flight method from the independent homogeneous agar phantom made from the agar solution of the same batch. In two-layer agar phantoms, the shear wave speeds of each layer were measured to be 11.8 ± 0.3 m/s (top layer, 3% agar) and 7.7 ± 0.2 m/s (bottom layer, 2% agar). In the three-layer agar phantom, the shear wave speeds of each layer were measured to be 11.6 ± 0.2 m/s, 7.8 ± 0.2 m/s and 3.3 ± 0.1 m/s for top (3% agar), middle (2% agar), and bottom layer (1% agar), respectively. All these measured shear wave speeds agree with the reference values (11.9 ± 1.5 m/s for 3% agar [14], 7.4 ± 0.3 m/s for 2% agar [15] and 3.9 ± 0.1 m/s for 1% agar [15]) in the literature.

TABLE I
ESTIMATED YOUNG'S MODULUS, REFERENCE VALUE AND INVERSION ERROR OF EACH LAYER

Phantom type		Two-layer phantom		
Top-layer thickness (mm)		0.45	1.00	2.00
Reference E (kPa)	T	420 ± 30		
	B	179 ± 13		
Estimated E (kPa) [Error (%)]	T	469 [11.6%]	454 [8.1%]	397 [-5.5%]
	B	135 [-24.8%]	156 [-13.1%]	139 [-22.5%]
Phantom type		Three-layer phantom		
Layer thickness (mm)		top layer: 0.63; middle layer: 1.10		
Reference E (kPa)	T	405 ± 20		
	M	183 ± 13		
	B	33 ± 3		
Estimated E (kPa) [Error (%)]	T	439 [8.4%]		
	M	217 [18.6%]		
	B	33 [0%]		

E: Young's modulus. T: top layer; M: middle layer, B: bottom layer.

The weighting function in the proposed WAPV inversion model was derived from the averaged weighting factor curve of all simulation data, which was inevitably different from the individual weighting factor curve. Therefore, the model inversion error changes with various layer thickness and shear

wave velocity configurations. For instance, in the two-layer agar phantom, the top-layer inversion error decreases from 11.6% (0.45 mm) to -5.5% (2.0 mm) as the layer thickness increases, meanwhile, the bottom-layer inversion error correspondingly changes with layer thickness from -24.8% (0.45 mm) to -22.5% (2.0 mm), as illustrated in Table I. To optimize the performance of the WAPV inversion model for different layer structures, a compensation on the model inversion error of each layer was proposed.

For two-layer materials, by assessing each simulation data with the WAPV inversion model, the inversion errors for different top-layer thickness from 0.1 mm to 2.0 mm and various top-bottom shear wave velocity ratios ($C_{S(top)}/C_{S(bottom)}$) from 1.14 to 8 were obtained, as shown in Fig. 3. As illustrated in the figure, the model inversion error changes with the top-layer thickness and top-bottom shear wave velocity ratio. For instance, Young's modulus inversion errors of a two-layer material with 0.5 mm top-layer thickness and a top-bottom shear wave velocity ratio of 2 are estimated to be 10.4% and -8.0% for the top and bottom layer, respectively.

Based on this pre-defined inversion error matrix, the Young's modulus inversion error in the two-layer material can then be compensated by adjusting the model-inversed Young's modulus using the predicted inversion error.

For layered materials with three or more number of layers, the same approach can be applied. However, it is time-consuming to obtain the full error matrix for multi-layered materials, since the number of simulations dramatically increases as the number of layer increases, even from 2 to 3. Thus, it is more realistic to evaluate the model inversion error of a multi-layered material in the region of interest. To do so, only the simulations with the pre-defined layer structure and speed ratio are solved, where the layer thickness could be assessed from the OCT structure image and speed ratio could be approximated from the inversed shear wave velocities of each layer. Then the model inversion error in the region of interest can be evaluated based on these simulations. Given the error matrix in the region of interest, the inversion error can then be compensated.
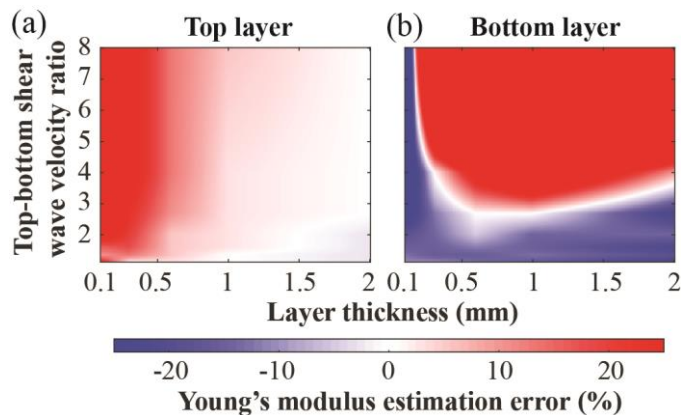

Fig. 3. Model inversion error as a function of top-layer thickness and top-bottom shear wave velocity ratio in a two-layer material for (a) top-layer inversion error and (b) bottom-layer inversion error.

In this experiment, the model inversion errors of two-layer agar phantoms were extracted from the error matrix shown in Fig. 3, while the model inversion error of the three-layer agar

phantom was evaluated from an additional simulation on a three-layer material, where the layer structure and shear wave velocity ratios were set to be the same as those measured in the experiment. The obtained Young's modulus inversion errors for two-layer and three-layer agar phantoms are summarised in Table II.

TABLE II
YOUNG'S MODULUS INVERSION ERROR FOR TWO-LAYER AND THREE-LAYER AGAR PHANTOMS

Phantom type		Two-layer phantom		
Top-layer thickness (mm)		0.45	1.00	2.00
Top-bottom-layer shear wave velocity ratio		1.53		
Model inversion error (%)	T	+10.8	+1.7	-2.5
	B	-14.2	-14.7	-21.5
Phantom type		Three-layer phantom		
Layer thickness (mm)		top layer: 0.63; middle layer: 1.10		
Top-middle-layer shear wave velocity ratio		1.5		
Middle-bottom-layer shear wave velocity ratio		2.5		
Model inversion error (%)	T	-2.5		
	M	+19.8		
	B	0		

T: top layer; M: middle layer; B: bottom layer.

TABLE III
ESTIMATED YOUNG'S MODULUS, REFERENCE VALUE AND INVERSION ERROR OF EACH LAYER AFTER COMPENSATION

Phantom type		Two-layer phantom		
Top-layer thickness (mm)		0.45	1.00	2.00
Reference E (kPa)	T	420 ± 30		
	B	179 ± 13		
Estimated E (kPa) [Error (%)]	T	432 [2.9%]	446 [6.2%]	407 [-3.1%]
	B	157 [-12.3%]	183 [2.2%]	177 [-1.1%]
Phantom type		Three-layer phantom		
Layer thickness (mm)		top layer: 0.63; middle layer: 1.10		
Reference E (kPa)	T	405 ± 20		
	M	183 ± 13		
	B	33 ± 3		
Estimated E (kPa) [Error (%)]	T	450 [11.1%]		
	M	181 [-1.1%]		
	B	33 [0%]		

T: top layer; M: middle layer; B: bottom layer.

The evaluated Young's moduli in Table I were then compensated according to the predicted model inversion errors in Table II, giving the compensated Young's modulus of each layer, as shown in Table III. As illustrated in the table, the Young's moduli got closer to the reference values after compensation. And the maximal total inversion error, e.g., the sum of the absolute value of the inversion error in each layer,

reduced to 15.2%. The remaining error in the evaluated Young's modulus was introduced by the other source during the model fitting process, such as biased fundamental mode SAW velocities (see Fig. 2(a, d)) in the reconstructed phase velocity dispersion curve, which was caused by the interference between the fundamental mode SAW and other high order wave modes. And this bias in the SAW phase velocity dispersion curve increase the uncertainty during the inversion, thus adding additional error in the evaluated depth-resolved Young's modulus.

B. In-vivo human skin experiment

Fig. 4 presents the representative flattened OCT structure images of normal *in-vivo* human skin at palm, back of hand and forearm after attenuation correction. Please note that the bright white band in the bottom of each subframe is the artifact after attenuation correction. For depth-resolved elasticity evaluation, the skin structure, e.g., layer thickness, needs to be pre-defined before inversion.
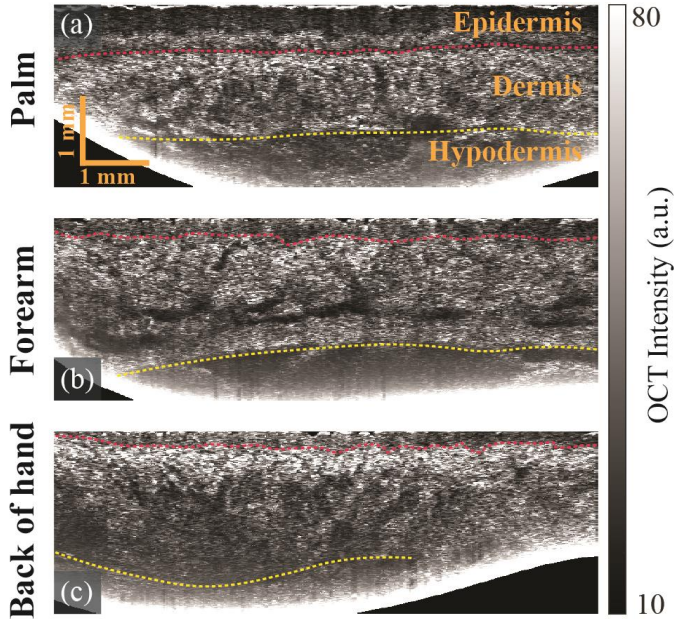

Fig. 4. Representative OCT structure images of normal in-vivo human skin at (a) palm, (b) back of hand and (c) forearm after surface flattened. Red and yellow dashed lines show the interface between epidermis/dermis and dermis/hypodermis, respectively.

The skin was modelled as a three-layer tissue in this study, e.g., epidermis, dermis, and hypodermis, with each layer assumed to be linear elastic and homogeneous. As skin structure varies in different sites, the boundaries of each layer were also defined differently based on [16]. In palm (Fig. 4(a)), epidermis layer was defined as the area between the surface and the first dark line in the structure image (denoted by a red dashed line in Fig. 4(a)). Dermis layer was defined as the area between the bottom boundary of epidermis layer (red dashed line) and the second dark line in the structure image (denoted by a yellow dashed line in Fig. 4(a)). The area below the bottom boundary of dermis layer was regarded as hypodermis layer. In forearm and back of hand, epidermis layer was the area from skin surface to the bottom boundary of the top dark area (denoted by a red dashed line in Fig. 4(b, c)). Dermis layer was

the area from the bottom boundary of epidermis layer (red dashed line) to the second boundary in the structure image (denoted by a yellow dashed line in Fig. 4(b, c)). The area below the bottom boundary of dermis layer was considered as hypodermis layer. In forearm, the interface between the dermis and hypodermis is faded, therefore, the thickness of dermis layer might be underestimated in some data.

TABLE IV
MEAN THICKNESS OF EPIDERMIS AND DERMIS LAYER OF SKIN AT DIFFERENT SITES

Skin site	Layer thickness (mm) [Mean ± Std.]			
	Epidermis		Dermis	
	Measured	Reference*	Measured	Reference*
Palm	0.27 ± 0.05	0.60 ± 0.01	0.73 ± 0.05	0.75 ± 0.16
Forearm	0.13 ± 0.02	0.10 ± 0.03	1.02 ± 0.06	1.08 ± 0.16
Back of hand	0.13 ± 0.02	0.19 ± 0.06	0.95 ± 0.07	0.93 ± 0.12

*Reference value was obtained from the literature [17].

Based on these definitions, the thickness of each layer was then assessed by pixel counting. The refraction indexes used for pixel-to-thickness conversion were 1.45 and 1.38 for epidermis and dermis, respectively [18, 19]. Table IV summarises the averaged thicknesses of the epidermis and dermis layer for the palm, forearm and back of hand from all subjects along with the corresponding reference values from the literature [17]. The mean thickness of the epidermis layer in palm is higher than that in forearm and back of hand, while the mean thickness of the dermis layer in palm is lower than that in forearm and back of hand. All quantified values agree well with those from the literature, except for the epidermis layer in palm. This discrepancy maybe caused by different locations on the palm selected between this study and the literature [17].
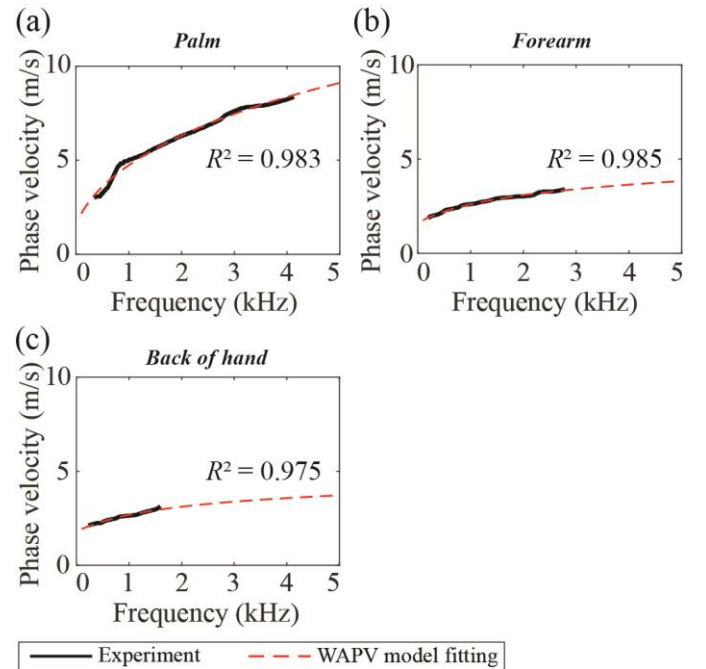

Fig. 5. Representative phase velocity dispersion curves (black solid lines) with their best WAPV model fitting curves (red dashed lines) overlaid for (a) palm, (b) forearm and (c) back of hand.

Fig. 5 demonstrates the representative phase velocity dispersion curves (black solid line) in palm, forearm and back of hand. The bandwidth of palm tissue is much wider than those on forearm and back of hand. The upper frequency reaches 4 kHz in palm, while in forearm and back of hand, the upper frequency only goes up to 3 kHz and ~2 kHz, respectively. Compared to forearm and back of hand, SAW is more dispersive in palm tissue. By substituting the assessed skin layer thicknesses and phase velocity dispersion curves into the WAPV inversion model, the Young's modulus of each layer was estimated. The red dashed lines in Fig. 5 depict the best fitting results with each has a R^2 value higher than 0.97.

Table V summaries the mean depth-resolved Young's modulus obtained from the WAPV model fitting for all subjects. For all skin types, the epidermis layer is the hardest while the hypodermis layer is the softest. The mean Young's modulus of epidermis and dermis layer in palm is higher than those in forearm and back of hand. However, the mean Young's modulus of hypodermis layer is close for all skin types.

TABLE V
MEAN DEPTH-RESOLVE YOUNG'S MODULUS OF SKIN AT DIFFERENT SITES

Skin site	Young's modulus (kPa) [Mean ± Std.]		
	Epidermis	Dermis	Hypodermis
Palm	927 ± 601	479 ± 171	6 ± 4
Forearm	214 ± 106	49 ± 26	11 ± 3
Back of hand	209 ± 67	40 ± 15	10 ± 4

TABLE VI
STATISTICAL ANALYSIS OF DEPTH-RESOLVED YOUNG'S MODULUS OF SKIN AT DIFFERENT SITES BETWEEN THE 20S AND THE 30S GROUP

Skin site	Skin layer	Young's modulus (kPa)		P value
		20s group	30s group	
Palm	Epidermis	748 ± 179	1224 ± 876	0.099
	Dermis	497 ± 196	449 ± 114	0.400
	Hypodermis	5 ± 3	8 ± 5	0.161
Forearm	Epidermis	170 ± 82	294 ± 97	**0.003**
	Dermis	34 ± 8	76 ± 25	**0.0003**
	Hypodermis	11 ± 3	13 ± 3	0.136
Back of hand	Epidermis	183 ± 61	255 ± 52	**0.002**
	Dermis	35 ± 10	48 ± 19	**0.048**
	Hypodermis	11 ± 3	8 ± 4	**0.009**

To evaluate the clinical relevance of the quantified depth-resolved elasticity, statistical analysis (two-tail student T-test) for two age groups (22-27 years old vs. 30-36 years old) was also performed in this study. The elasticity difference in gender was not compared as previous study suggests that there is no difference in the mechanical property between male and female with similar age [20]. Table VI presents the results of the statistical analysis. The mean Young's modulus of the epidermis and dermis layer of forearm and back of hand is significantly higher in the 30s group than that in the 20s group. Additionally, the mean Young's modulus of the hypodermis layer of back of hand is significantly lower in the 30s group than that in the 20s group.

V. DISCUSSION

In this paper, a novel and reliable inversion model, termed WAVP inversion model, for depth-resolved elasticity evaluation in multi-layered soft tissues was proposed. The proposed inversion model was firstly validated in multi-layered agar phantoms and then demonstrated in human skin *in-vivo*.

Compared to the wavelength-depth inversion model employed in our previous studies [5-7], the proposed WAPV model has the following advantages: 1) the minimum depth that can be assessed by this model is not limited by the up frequency in the phase velocity dispersion curve, as the depth-resolved elasticity was evaluated by matching the measured phase velocity dispersion curve with the one that generated from an empirical mathematic forward model. Therefore, the Young's modulus of epidermis layer, which typically cannot be assessed through the conventional wavelength-depth inversion model, can be estimated in this model as well; 2) better inversion accuracy. The conventional wavelength-depth inversion model is only capable of providing accurate Young's modulus estimate in the top layer as the phase velocity stabilise at the Rayleigh wave speed of the top layer when the SAW wavelength is less than the top-layer thickness. For the elasticity of the second layer to the bottom layer, the conventional model could only approximate because of the dispersive behaviour of SAW. However, the results of the multi-layered agar phantom experiment suggest that the WAPV inversion model is able to provide accurate elasticity estimates with an inversion error up to 24.8% in each layer (Table I) before model inversion error compensation, and a maximal total inversion error (a sum of the inversion error in each layer) of 15.2% in each sample (Table III) after model inversion error compensation.

In the *in-vivo* human skin experiment, due to the individual differences in skin structure and the limited bandwidth in the phase velocity dispersion curve, it is difficult to obtain the exact model inversion error of each layer for every subject. Thus, no model inversion error compensation was performed.

To validate the quantified results, we converted the quantified depth-resolved Young's modulus E_{layer} to bulk Young's modulus E_{bulk} first and compared them with reference values in the literature, where the conversion was through a weighted averaged according to the layer thickness h:

$$E_{bulk} = \frac{E_{epi} \cdot h_{epi} + E_{der} \cdot h_{der} + E_{hypo} \cdot h_{hypo}}{h_{epi} + h_{der} + h_{hypo}} \qquad (8)$$

The thickness of hypodermis layer was assumed to be 1.91 mm [21] for all types of skin during the conversion.

Table VII summaries the calculated bulk Young's modulus of skin at each site and the corresponding reference values from the literature. As illustrated in the table, the quantified values are on the same order of magnitude as the reference values. However, as the mechanical property of skin is associated with several factors, i.e., age, measurement direction and strain amount, there are discrepancies among the values quantified in this study and those from the literature.

TABLE VII
BULK YOUNG'S MODULUS OF SKIN AT DIFFERENT SITES AND THE
CORRESPONDING REFERENCE VALUES FROM THE LITERATURE

Palm				
Source	Number of subjects	Age	Young's modulus (kPa)	Method
Experiment	**11**	**22-36**	**212 ± 78**	**depth-resolved SAW-OCE**
Zhang [2]	10	46-61	108 ± 48	SAW elastography
Forearm				
Source	Number of subjects	Age	Young's modulus (kPa)	Method
Experiment	**11**	**22-36**	**32 ± 11**	**depth-resolved SAW-OCE**
Zhang [2]	10	46-61	42 ± 32	SAW elastography
Wakhlu [22]	16	41 ± 12	16 – 26	ultrasound elastography
Boyer [23]	4	23-28	13 - 33	dynamic indentation
Diridollou [24]	10	20-30	129 ± 88	suction test
Agache [3]	141	3-89	420 - 850	torsion test
Back of hand				
Source	Number of subjects	Age	Young's modulus (kPa)	Method
Experiment	**11**	**22-36**	**29 ± 8**	**depth-resolved SAW-OCE**
Wakhlu [22]	16	41 ± 12	11 - 23	ultrasound elastography

The aging process has a profound effect on the structure of the elastic fiber system in skin, thus changing its mechanical property [25]. For both chronic 'intrinsically' aged skin (aging caused by normal metabolic process) and 'extrinsically' aged skin (aging caused by exposed to ultraviolet light), the ability of skin to recoil is significantly reduced, resulting in an increase in the skin stiffness [26-28].

Besides, skin is found to be highly anisotropic. The Young's modulus of skin is dependent on the measurement orientation with respect to Langer's lines, i.e., the natural orientation of collagen fibers in the dermis layer, and the highest value can be seen in the parallel direction, which is approximately twice the values in the perpendicular orientation [29-31]. This may explain why the evaluated Young's modulus of palm and back of hand in this study is higher than the reference values even though the age of subjects in this study is lower than that in the literature.

In addition, the mechanical response of skin is non-linear and depends on the strain mount because of its microstructural constituents [32]. At low strain levels (0 ~ 0.3), skin is relatively soft as the response of skin is carried through the elastic components instead of collagen fibers [32]. At higher strain level (0.3 ~ 0.6), the stiffness of skin increases rapidly since the collagen fibers are straightened and begin to carry the major part of the load [33]. If the strain is larger than 0.6, all collagen fibers are straight, and skin reaches its highest Young's modulus [32]. Therefore, in forearm, the measured Young's modulus in this study (low strain amount) is similar to

that from SAW and ultrasound elastography (low strain amount). However, the quantified values are much lower than those from mechanical tests, such as suction test and torsion test (high strain level).

The statistical analysis on Young's modulus of each skin layer between subjects with two age groups (20s vs. 30s) suggests the elasticity of epidermis and dermis layer of forearm and back of hand increases with advancing age, which agrees with the conclusions in [26-28]. However, in hypodermis layer of back of hand, the statistical analysis shows a decreasing trend in elasticity with increasing age. This result may also be reasonable as the phase velocity dispersion curve is steeper in 30s than 20s, thus, the inversion model tends to give smaller phase velocity estimates in the third layer, i.e., hypodermis layer. Nonetheless, further study needs to confirm this result because there has yet been literature so far about the elasticity change with age in each layer of skin.

There are also limitations in the proposed WAPV inversion model. One limitation is that it needs prior knowledge of the layer thickness. Therefore, the penetration depth of the optical imaging system (up to 1.5 mm in soft tissue) limits the types of biological soft tissue that the model can be applied on. By combining other imaging modality (i.e., ultrasound imaging) for layered structure assessment, the elasticity of the tissue located below human skin has the potential to be evaluated. Nevertheless, the maximum resolvable depth of this method was fundamentally limited by the penetration depth of the generated SAW in tissues.

Another limitation is that it is sensitive to the artifacts in the measured phase velocity dispersion curve, e.g., biased fundamental mode phase velocities at some frequencies caused by the interference of the fundamental mode SAW and SAW in other high order modes. In this study, we manually picked and removed the phase velocities obtained from high order SAW modes in the fitting to minimize their impacts (Fig. 2(d)).

In this study, the SAW was induced in a contact way using a piezoelectric actuator. The surface loading introduced by the actuator head may generate largely localized deformations on the sample surface, resulting in the stiffness of the surrounding area increasing and potentially adding additional error to the evaluated top-layer Young's modulus. A variety of non-contact loading method developed recently, such as air-coupled focused-ultrasound transducer [34] and air-puff system [35], might help to solve this problem. Additionally, the bandwidth of the induced SAW in skin was measured to be less than 4 kHz, which increased the inversion uncertainty for the top layer (requiring high frequency information). To mitigate this problem, an excitation source with finer focus can be employed in the future to extend the bandwidth of the generated SAW in the soft tissue.

Although the results of statistical analysis agree with conclusions from other literatures, the results may not be representative due to the limited subjects in each group (7 subjects in 20s group, 4 subjects in 30s group). Hence, a larger-scale study is required to do in the future to further confirm the preliminary results obtained in this study.

VI. CONCLUSION

This study proposed a new weighted average phase velocity

(WAPV) inversion model for depth-resolved Young's modulus evaluation in layered biological soft tissues for SAW elastography. The forward model for the SAW phase velocity curve generation was derived from the numerical solutions of the wave equations describing the propagation of SAW in layered materials, and the inversion was implemented by matching the measured phase velocity dispersion curve to the one generated from the forward model using the least squares fitting. Three two-layer agar phantoms with different top-layer thicknesses and one three-layer agar phantom were tested to validate the proposed inversion model. The model was also demonstrated on human skin at various sites (palm, forearm and back of hand) *in-vivo*. The results show the proposed inversion model has the capability of providing accurate depth-resolved Young's modulus estimates with up to 15.2% total inversion error/per sample in multi-layer tissue mimicking materials. In *in-vivo* human skin, the bulk Young's modulus quantification results (palm: 212 ± 78 kPa; forearm: 32 ± 11 kPa and back of hand: 29 ± 8 kPa) are also comparable to the reference values in the literature. Therefore, the proposed model has great potential to be applied in the real skin disease diagnosis in the future.

REFERENCES

[1] Lawton, S., *Skin 1: the structure and functions of the skin.* Nursing Times[online], 2019. **115**(12): p. 30-33.

[2] Zhang, X., et al., *Quantitative assessment of scleroderma by surface wave technique.* Med Eng Phys, 2011. **33**(1): p. 31-7.

[3] Agache, P.G., et al., *Mechanical properties and Young's modulus of human skin in vivo.* Arch Dermatol Res, 1980. **269**(3): p. 221-32.

[4] Cua, A., K.-P. Wilhelm, and H. Maibach, *Elastic properties of human skin: relation to age, sex, and anatomical region.* Archives of Dermatological Research, 1990. **282**(5): p. 283-288.

[5] Li, C., et al., *Determining elastic properties of skin by measuring surface waves from an impulse mechanical stimulus using phase-sensitive optical coherence tomography.* Journal of The Royal Society Interface, 2012. **9**(70): p. 831-841.

[6] Li, C., et al., *Quantitative elastography provided by surface acoustic waves measured by phase-sensitive optical coherence tomography.* Optics letters, 2012. **37**(4): p. 722-724.

[7] Zhou, K., et al., *High-intensity-focused ultrasound and phase-sensitive optical coherence tomography for high resolution surface acoustic wave elastography.* Journal of biophotonics, 2018. **11**(2): p. e201700051.

[8] Krebes, E., *Seismic forward modeling.* CSEG Recorder, 2004. **30**: p. 28-39.

[9] Leong, E.C. and A.M.W. Aung, *Weighted average velocity forward modelling of Rayleigh surface waves.* Soil Dynamics and Earthquake Engineering, 2012. **43**: p. 218-228.

[10] Mohan, K.D. and A.L. Oldenburg, *Elastography of soft materials and tissues by holographic imaging of surface acoustic waves.* Optics express, 2012. **20**(17): p. 18887-18897.

[11] Rix, G.J., *Near-surface site characterization using surface waves*, in Surface Waves in Geomechanics: Direct and Inverse Modelling for Soils and Rocks. 2004, Springer. p. 1-46.

[12] Li, C., et al., *Depth evaluation of soft tissue mimicking phantoms using surface acoustic waves.* Physics Procedia, 2015. **63**: p. 177-181.

[13] Song, S., et al., *Shear modulus imaging by direct visualization of propagating shear waves with phase-sensitive optical coherence tomography.* Journal of biomedical optics, 2013. **18**(12): p. 121509.

[14] Li, C., Z. Huang, and R.K. Wang, *Elastic properties of soft tissue-mimicking phantoms assessed by combined use of laser ultrasonics and low coherence interferometry.* Optics express, 2011. **19**(11): p. 10153-10163.

[15] Hamhaber, U., et al., *Comparison of quantitative shear wave MR‐elastography with mechanical compression tests.* Magnetic Resonance in Medicine: An Official Journal of the International Society for Magnetic Resonance in Medicine, 2003. **49**(1): p. 71-77.

[16] Adabi, S., et al., *Universal in vivo textural model for human skin based on optical coherence tomograms.* Scientific reports, 2017. **7**(1): p. 1-11.

[17] Lee, Y. and K. Hwang, *Skin thickness of Korean adults.* Surgical and radiologic anatomy, 2002. **24**(3-4): p. 183-189.

[18] Lister, T., P.A. Wright, and P.H. Chappell, *Optical properties of human skin.* Journal of biomedical optics, 2012. **17**(9): p. 090901.

[19] Ding, H., et al., *Refractive indices of human skin tissues at eight wavelengths and estimated dispersion relations between 300 and 1600 nm.* Physics in Medicine & Biology, 2006. **51**(6): p. 1479.

[20] Rahrovan, S., et al., *Male versus female skin: What dermatologists and cosmeticians should know.* International journal of women's dermatology, 2018. **4**(3): p. 122-130.

[21] Hwang, K., H. Kim, and D.J. Kim, *Thickness of skin and subcutaneous tissue of the free flap donor sites: a histologic study.* Microsurgery, 2016. **36**(1): p. 54-58.

[22] Wakhlu, A., et al., *Assessment of extent of skin involvement in scleroderma using shear wave elastography.* Indian Journal of Rheumatology, 2017. **12**(4): p. 194.

[23] Boyer, G., et al. *In vivo characterization of viscoelastic properties of human skin using dynamic micro-indentation*. in *2007 29th Annual International Conference of the IEEE Engineering in Medicine and Biology Society*. 2007. IEEE.

[24] Diridollou, S., et al., *In vivo model of the mechanical properties of the human skin under suction.* Skin Research and technology, 2000. **6**(4): p. 214-221.

[25] Sherratt, M.J., *Age-related tissue stiffening: cause and effect.* Advances in wound care, 2013. **2**(1): p. 11-17.

[26] Smalls, L.K., R. Randall Wickett, and M.O. Visscher, *Effect of dermal thickness, tissue composition, and body site on skin biomechanical properties.* Skin research and technology, 2006. **12**(1): p. 43-49.

[27] Takema, Y., et al., *Age-related changes in the elastic properties and thickness of human facial skin.* British Journal of Dermatology, 1994. **131**(5): p. 641-648.

[28] Escoffier, C., et al., *Age-related mechanical properties of human skin: an in vivo study.* Journal of Investigative Dermatology, 1989. **93**(3).

[29] Kalra, A., A. Lowe, and A.A. Jumaily, *An overview of factors affecting the skins Youngs modulus.* Journal of Aging Science, 2016.

[30] Annaidh, A.N., et al., *Characterization of the anisotropic mechanical properties of excised human skin.* Journal of the mechanical behavior of biomedical materials, 2012. **5**(1): p. 139-148.

[31] Ottenio, M., et al., *Strain rate and anisotropy effects on the tensile failure characteristics of human skin.* Journal of the mechanical behavior of biomedical materials, 2015. **41**: p. 241-250.

[32] Joodaki, H. and M.B. Panzer, *Skin mechanical properties and modeling: a review.* Proceedings of the Institution of Mechanical Engineers, Part H: Journal of Engineering in Medicine, 2018. **232**(4): p. 323-343.

[33] Daly, C., *The role of elastin in the mechanical behavior of human skin.* Proceedings of the 8th Inr. Confi Med. Biol. Engr, 1969: p. 18-27.

[34] Ambroziński, Ł., et al., *Acoustic micro-tapping for non-contact 4D imaging of tissue elasticity.* Scientific reports, 2016. **6**: p. 38967.

[35] Wang, S. and K.V. Larin, *Noncontact depth-resolved micro-scale optical coherence elastography of the cornea.* Biomedical optics express, 2014. **5**(11): p. 3807-3821.

[36] Kirby, M.A., et al., *Spatial resolution in dynamic optical coherence elastography.* Journal of biomedical optics, 2019. **24**(9): p. 096006.